Title	Crystal chemistry of melilite [CaLa]2[Ga]2[Ga2O7]2 : a five dimensional solid electrolyte
Author(s)	Wei, Fengxia; Baikie, Tom; An, Tao; Kloc, Christian; Wei, Jun; White, Timothy John
Citation	Wei, F., Baikie, T., An, T., Kloc, C., Wei, J., & White, T. (2012). Crystal chemistry of melilite [CaLa]2[Ga]2[Ga2O7]2 : a five dimensional solid electrolyte. Inorganic chemistry, 51(10), 5941-5949.
Date	2012
URL	http://hdl.handle.net/10220/11600
Rights	© 2012 American Chemical Society. This is the author created version of a work that has been peer reviewed and accepted for publication by Inorganic chemistry, American Chemical Society. It incorporates referee's comments but changes resulting from the publishing process, such as copyediting, structural formatting, may not be reflected in this document. The published version is available at: [http://dx.doi.org/10.1021/ic300585t].

The crystal chemistry of melilite $[CaLa]_2[Ga]_2[Ga_2O_7]_2$: a five dimensional solid electrolyte

Fengxia Wei [a*], Tom Baikie[a], Tao An[a], Christian Kloc[a], Jun Wei[c], Tim White[a,b*]

[a] Division of Materials Science & Engineering, Nanyang Technological University, Singapore

[b] Centre for Advanced Microscopy, Australian National University, Sullivan's Creek Road, Canberra, ACT 2601 Australia

[c] Singapore Institute of Manufacturing Technology, 71 Nanyang Drive, Singapore

* Corresponding author: weif0002@ntu.edu.sg; tjwhite@ntu.edu.sg

Abstract

Melilite-type $[A_2]_2[B^I]_2[B^{II}_2O_7]_2$ gallates are promising ion conducting electrolytes for deployment in solid oxide fuel cells. Single crystals of $[CaLa]_2[Ga]_2[Ga_2O_7]_2$, grown in an optical floating zone furnace, were investigated using a combination of transmission electron microscopy and single crystal X-ray diffraction. Strong anisotropic displacements of oxygen arise from the structural misfit between the interlayer Ca/La cations and the $[Ga]$-$[Ga_2O_7]$ tetrahedral layers. A model employing two-dimensional modulation achieves bond lengths and bond angles that preserve satisfactory bond valence sums throughout the structure. The melilite belongs to the tetragonal superspace group $P\bar{4}2_1m(\alpha,\alpha,0)00s(\bar{\alpha},\alpha,0)000$, $\alpha = 0.2160(5)$, with a subcell metric of $a = 7.9383(2)$ Å, $c = 5.2641(3)$ Å, onto which modulation vectors are superimposed: $\boldsymbol{q_1} = \alpha\,(\boldsymbol{a^*} + \boldsymbol{b^*})$, $\boldsymbol{q_2} = \alpha\,(-\boldsymbol{a^*} + \boldsymbol{b^*})$. Both displacive (cation and anion) and occupational (cation) modulations contribute to incommensuration. The analysis of structural adjustments that accompany changes in temperature and composition provides assurance that the crystal chemical model is correct. By better understanding the flexibility of this modulated structure a rational approach towards crystallochemical optimization of electrolyte performance by enhancing oxygen mobility becomes feasible.

1. Introduction

The drive towards sustainable energy production and conservation supports the expansion of fuel cell technologies, particularly solid oxide fuel cells (SOFC). For these devices, a key requirement is an electrolyte possessing high oxide ion conductivity at moderate temperature (<800°C). To date, electrolyte research and deployment overwhelmingly targets fluorite- and perovskite-type oxides, e.g. stabilised zirconia (0.01 Scm^{-1} at 700°C) or doped $LaGaO_3$ (0.1 Scm^{-1} at 800°C), where oxygen transport is mediated by vacancy defects.[1-5] However, apatites (e.g. $La_{10}Ge_{5.5}W_{0.5}O_{27.5}$ 0.02 Scm^{-1} at ~800°C) and fergusonites (e.g. $CeNbO_{4+\delta}$ 0.03 Scm^{-1} at 800°C) containing mobile super-stoichiometric oxygen draw growing interest.[6-11] Recently, layered melilite structures containing gallium oxide tetrahedral moieties (GaO_4) have been proposed as alternative, lower temperature solid electrolyte materials. For example, $[Sr_{0.46}La_{1.54}]_2[Ga]_2[Ga_2O_{7.27}]_2$ displays an ionic conductivity of 0.02 to 0.1 Scm^{-1} from 600 to 900°C.[12, 13] The melilite structural framework can accommodate a large excess of oxygen, up to 0.32 per formula unit (e.g. $[Ca_{0.36}La_{1.64}]_2[Ga]_2[Ga_2O_{7.32}]_2$),[13] and these interstitial oxide ions are believed to be highly mobile.

The melilite substructure conforms to tetragonal $P\bar{4}2_1m$ symmetry, yielding the ideal formula $[A_2]_2[B^I]_2[B^{II}_2O_7]_2$, where A is a large divalent alkali earth (AE^{2+}) or trivalent lanthanide (Ln^{3+}) and B^I, B^{II} are symmetrically distinct small cations (e.g. Si^{4+}, Ga^{3+}, Zn^{2+}, Co^{2+} and Ge^{4+}) (Figure 1). Two dimensional layers are created by corner-connection of $B^I O_4$ tetrahedra and $B^{II}_2O_7$ tetrahedral dimmers, separated by A cations. Misfit between

the tetrahedral layers and the interlayer cations is accommodated by atomic displacements leading to basal plane incommensuration in natural and synthetic melilites.[14-21] Compositions showing promise as SOFC electrolytes have not been deeply investigated and many outstanding questions remain regarding the correlation of modulation with excess oxygen content and conductivity. Recently, we described a new incommensurate melilite structure $[CaNd]_2[Ga]_2[Ga_2O_7]_2$ [22] and found that substitution of Nd by La leads to systematic adjustment of the modulation vector. In this related structural study of $[CaLa]_2[Ga]_2[Ga_2O_7]_2$, a combination of single crystal X-ray diffraction and transmission electron microscopy confirmed a (3+2) dimensional incommensurate structure that can be rigorously described using superspace group formalism.[23] This quantitative description of melilite modulation and its correlation with composition provides guidance for optimizing the crystal chemical design of melilite electrolytes.
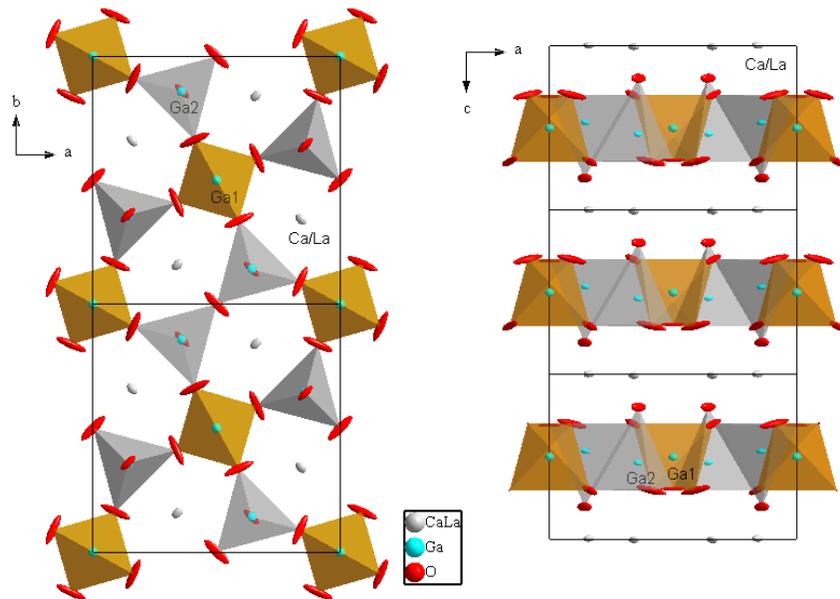

Figure 1. The average 3D structure of $[CaLa]_2[Ga]_2[Ga_2O_7]_2$ obtained from single crystal X-ray diffraction. Ellipsoids are drawn with 50% probability.

2. Experimental

Single crystal growth

Single crystals of $[CaLa]_2[Ga]_2[Ga_2O_7]_2$ were grown using an optical floating zone furnace (FZ-T-4000-H-VPO-VII-PC, Crystal Systems Corporation, Japan). A precursor powder (10 grams) containing a stoichiometric mixture of La_2O_3 (99.998% Alfa Aesar), $CaCO_3$ (99.9%, Alfa Aesar) and Ga_2O_3 (99.999%, Aldrich) was ground and homogenized in ethanol, dried in air (100°C/6 hours), then fired (800°C/10 hours) to decompose $CaCO_3$. The La_2O_3 was dehydrated and decarbonated (1000°C/10 hours) before use. The calcines were reground, pressed into pellets and sintered (1400 °C/12 hours/air) to yield a single phase product. The polycrystalline mass was isostatically pressed into duplicate cylinders (5cm × 0.5cm), that were sintered (1400°C/12 hours), to serve as the feed and seed rods before mounting in the mirror furnace. The optical floating zone furnace was equipped with four 1.5 kW halogen lamps, with corresponding ellipsoidal mirrors to focus the infrared irradiation to a small region, while a constant flow of dry air (2 L/min) passed through the chamber during the crystal growth. With the onset of melting, the tips of the feed and seed rods were brought into contact to form the floating-zone, and upon stabilisation, the entire mirror stage was raised at a rate of 5 mm/h for crystal growth. The rods were counter-rotated at constant speed (30 rpm) to maintain a stable and well-mixed molten zone. Total growth time was around 8 hours. Single crystals of $[CaLa]_2[Ga]_2[Ga_2O_7]_2$ up to 2mm long were obtained, and are similar in appearance to those of $[CaNd]_2[Ga]_2[Ga_2O_7]_2$,[22] but more difficult to prepare as the

blue colour in the latter better absorbs infrared radiation and simplifies the crystal growth process. For both compositions, crack propagation during cooling was exacerbated by crystallographic stresses arising from misfit of the tetrahedral network and the interlayer cations which limits crystal size.

Structural characterisation

Single crystal diffraction. A single crystal shard (0.1mm×0.12mm×0.15mm) was cleaved and mounted on a glass fibre. Data was collected using a Bruker Smart Apex II single crystal diffractometer (X-ray radiation Mo *Kα*, λ=0.71073Å), over an angular range of 2.08°≤θ≤37.84°, with an exposure time of 200s/degree to give a total collection time of ~48 hours that ensures the weaker satellite reflections are recorded. The modulation vectors were calculated by the least-squares method from 1876 satellite reflections. The Saint module, deployed within Apex II, was used for reflection integration, performing Lorentz polarisation and multi-scan absorption corrections. The data were treated using Jana 2006 [24] without additional absorption correction. As a two-dimensionally modulated structure, all reflections for $[CaLa]_2[Ga]_2[Ga_2O_7]_2$, were indexed using five integers (*h k l m n*): $\mathbf{H} = h\mathbf{a}^* + k\mathbf{b}^* + l\mathbf{c}^* + m\boldsymbol{q}_1 + n\boldsymbol{q}_2$, where $\boldsymbol{a}^*$, $\boldsymbol{b}^*$ and $\boldsymbol{c}^*$ are the reciprocal lattice vectors. The modulation vectors $\boldsymbol{q}_1 = 0.2160(5)$ $(\boldsymbol{a}^* + \boldsymbol{b}^*)$, $\boldsymbol{q}_2 = 0.2160(5)$ $(-\boldsymbol{a}^* + \boldsymbol{b}^*)$ were determined from 908 main reflections, 1598 first order and 278 second order satellite reflections. Experimental and structural analysis details are collected in Table 1.

Table 1. Experimental details

Crystal data	
Chemical formula	$Ca_{1.033}La_{0.967}Ga_3O_7$
Chemical formula weight	493.50
Temperature (K)	293
Cell Setting	Tetragonal

Superspace group	$P\bar{4}2_1m(\alpha,\alpha,0)00s(\bar{\alpha},\alpha,0)000$
a (Å)	7.9386(2)
c (Å)	5.2641(3)
Volume (Å^3)	331.75(3)
Formula units (Z)	2
D_x (Mg m^{-3})	4.939
Modulation wave vectors	$q_1 = 0.2160(5)$ $(a^* + b^*)$
	$q_2 = 0.2160(5)$ $(-a^*+b^*)$
Crystal form	Irregular
Crystal size (mm)	$0.10 \times 0.12 \times 0.15$
Crystal colour	Colorless
Data collection	
Diffractometer	Bruker Smart ApexII Three circle diffractometer
Radiation type	Mo $K\alpha$
Wavelength (Å)	0.71073
Absorption correction type	Multi-scan
Absorption coefficient μ (mm^{-1})	18.753
Range of h, k, l, m, n	$-11 \rightarrow h \rightarrow 13$
	$-13 \rightarrow k \rightarrow 13$
	$-8 \rightarrow l \rightarrow 9$
	$-1 \rightarrow m \rightarrow 1$
	$-1 \rightarrow n \rightarrow 1$
No. of measured reflections	40878
No. of unique reflections	7622
No. of observed reflections	2784
No. of main reflections	908
No. of satellites	
For $\pm(1, 0) \pm(0, 1)$	1598
For $\pm (1, 1) \pm (-1, 1)$	278
Criterion for observed reflections	$I > 3\sigma (I)$
Refinement	
Refinement on	F
R, wR (all reflections)	0.0568, 0.0851
R, wR (main reflections)	0.0319, 0.0468
R, wR (satellites) for $\pm(1, 0) \pm(0, 1)$	0.1170, 0.1324
For $\pm (1, 1) \pm (-1, 1)$	0.2230, 0.2592
S	3.70
No. of parameters	333
Weighting scheme	$w = [\sigma^2(F) + (0.01F)^2]^{-1}$
$(\Delta/\text{s.u.})_{max}$	0.0494
$\Delta\rho_{max}$ (e Å^{-3})	2.97
$\Delta\rho_{min}$ (e Å^{-3})	-2.98
Extinction correction	B-C type 1 Lorentzian isotropic (Becker &

	Coppens, 1974)
Extinction coefficient	3400(400)
Source of atomic scattering factors	International Tables for Crystallography (1992, Vol.C) [25]

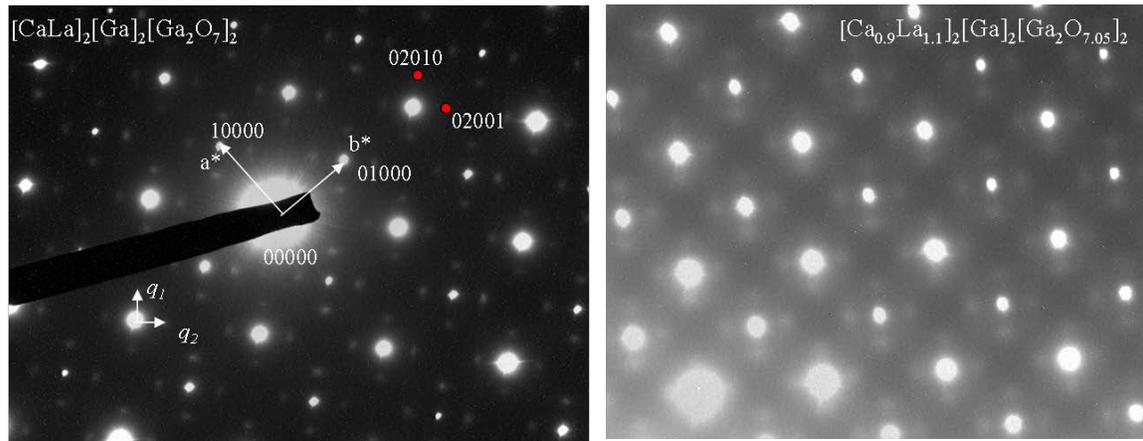
Figure 2. SAED pattern along <001> with each reflections indexed by five integer values including q_1 and q_2. The satellite intensity becomes weaker and diffuse as the content of La over Ca increases.

Transmission electron microscopy. Selected area electron diffraction patterns (SAED) of single crystals (Figure 2) were obtained using a transmission electron microscope JEOL 2100F operated at 200 kV and fitted with a Gatan Ultra CCD camera. The crystal was crushed and ground under ethanol, then deposited on holy carbon coated films supported by a copper grid. The preferred cleavage favours the [100] zone, rather than [001] where satellites are most evident in SAED and direct measurement of q_1/ q_2 is possible. A Gatan double tilt holder was employed to observe the principle crystallographic orientations, and to reduce rapid beam damage, data were collected with a defocused electron beam. The satellite reflections were extremely weak and long exposure time (up to 80s) was required to digitally record these features; only first order satellites were observed, and in [001] zones, these form a square around the principle reflections. The

modulation vectors $q_1 = 0.23 (a^* + b^*)$, $q_2 = 0.23(-a^* + b^*)$, are comparable to those obtained from single crystal diffraction.

3. Symmetry and Structure Determination

The (3+2)-dimensional incommensurate structure can be considered a 3-dimensional physical object combined with 2 higher dimensions, and the corresponding superspace group contains the symmetry of the 3D substructure, plus the symmetry elements of the higher dimension. Recently, Stokes *et al.*[23] have derived all the (3+2) superspace groups, and suggested an extended formalisation. Accordingly, [CaLa]$_2$[Ga]$_2$[Ga$_2$O$_7$]$_2$ adopts the melilite basic metric $a = 7.9383(2)$, $c = 5.2641(3)$Å with two incommensurate modulation vectors: $q_1 = 0.2160(5)(a^*+b^*)$, $q_2 = 0.2160(5)(-a^*+b^*)$, resulting in a superspace group $P\bar{4}2_1m(\alpha,\alpha,0)00s(\bar{\alpha},\alpha,0)000$, where $\alpha = 0.2160(5)$ is the magnitude of modulation vectors, and s (=1/2) indicates an intrinsic translation in the fourth direction.

To determine the (3+2)D structure, modulation of both atomic positions and displacement parameters (ADP) were applied using the satellite reflections (1, 0), (0, 1), (1, 1) and (-1, 1). The number of observed 2nd order satellites was small (278 for I>3σ) and due to the fact that $\alpha \sim 1/4$, the satellites (*h, k, l*, 1, 1), (*h*+1*, k, l*, -1, 1), (*h, k, l*, 1, -1) (*h, k*+1*, l*, -1, -1) overlap, leading to a relatively high R^{2nd}_{obs} factor (~0.22). An overlap correction was applied by treating pairs of combined satellites as fully overlapped reflections. R^{2nd}_{obs} can be reduced by ~15% with overlap correction. Occupancy modulation was also applied for Ca/La, which is refined before the positional modulation to minimize the coupling of

modulation parameters. Both harmonic and unharmonic ADP modulations have been attempted, according to model from Li *et. al.*,[26] similar results can be obtained by refining ADPs by 4 harmonic waves combined with 2 unharmonic waves, and refining ADPs by 6 harmonic waves. Further inclusion of unharmonic ADP modulation can significantly reduce the R factor, but is in expense of bond valence summations. Only harmonic ADPs are refined here to minimize the complexity of the model.

4. Discussion

Average structure

In the average structure, Ca/La cations are statistically dispersed between the GaO_4 tetrahedral layers and align as strings along [001] that are co-axial with the pentagonal channels formed by the GaO_4 tetrahedra (Figure 1). A strong anisotropy of the La/Ca and O displacement ellipsoids is observed in the *ab* plane. The O2 site has the longest ellipsoidal axis directed along <110>. Ga^{II}-O2-Ga^{II} is linearly bonded on average, but the large ADP of O2 perpendicular to the Ga^{II}-O2 vector suggests flexing of the Ga^{II}-O2 bonds. This observation is consistent with twisting of the $Ga^{II}_2O_7$ tetrahedral dimers around <001>, accommodated by a slight rotation of the $Ga^{I}O_4$ tetrahedra, also around <001>. Almost all the oxygen ellipsoids elongate towards the *A* site positions, due to the size misfit between the interstices (volume = ~30.34Å^3) and the Ca/La ionic size. In this manner, the flexible framework is primed to accommodate a large amount of interstitial oxygen, and consequently, for the $[Ca_{1-x}La_{1+x}]_2[Ga]_2[Ga_2O_{7+x/2}]_2$ average structures, phase transitions from tetragonal ($x \leq 0.5$) to orthorhombic ($0.5 < x \leq 0.6$) to triclinic

symmetry ($0.6 < x \leq 0.64$) were observed as lanthanum content increased.[13] Furthermore, those electrolytes with $x > 0.5$ gave lower conductivities attributable to the reduction of symmetry that created more intricate diffusion paths, show higher activation energies and poorer mobility. The correlation of lower symmetry and inferior electrolyte performance is common to melilites, apatites and fergusonites.[7, 27, 28]

Table 2. Atomic coordinates and isotropic ADP for the $P\bar{4}2_1m$ average structure of $[CaLa]_2[Ga]_2[Ga_2O_7]_2$

Atoms	x	y	z	$Biso$	occupancy
La^I	0.34137(5)	0.15863(5)	0.00415(12)	0.01045(14)	0.4684
Ca^I	0.34137(5)	0.15863(5)	0.00415(12)	0.01045(14)	0.5316
Ga^I	0	0	0	0.0094(2)	1
Ga^{II}	0.14327(6)	0.35673(6)	0.46517(15)	0.00753(14)	1
O1	0.1409(5)	0.3591(5)	0.8041(11)	0.0188(11	1
O2	0.5	0	-0.693(2)	0.044(3)	1
O3	0.0898(13)	0.1626(7)	0.2970(10)	0.044(2)	1

Modulated Structure

In (3+2) D structures, two additional parameters t and u are introduced, besides the x, y, z atomic fractional coordinates, to represent the fourth and fifth coordinates in the higher dimensions. Atomic displacements along t and u can be very different, which necessitates the validation of modulation with respect to A-O bond variation, GaO_4 tetrahedral distortion (table 3), occupancy modulation of Ca/La, bond valance summation, and temperature dependence. The flexible A-O and Ga-O polyhedra enable the accommodation and relaxation of interstitial oxygen and enhance its migration.[12]

Table 3. Modulated structure: Interatomic distances (Å) and tetrahedral angles (°)

	average	minimum	maximum
A-O polyhedra			
A-O1-iii	2.50(5)	2.38(5)	2.62(5)
A-O1-v	2.57(5)	2.42(5)	2.67(4)

A-O1-ii	2.58(5)	2.42(5)	2.67(5)
A-O2-i	2.31(5)	1.99(6)	2.62(5)
A-O3-iv, viii	2.53(6)	2.40(6)	2.63(6)
A-O3-v,vii	2.87(6)	2.66(6)	3.08(6)
Ga^IO_4 tetrahedra			
Ga^I- O3	1.84(6)	1.63(5)	2.04(5)
O3-i(i/ii/iv)—Ga^I—O3-ii (v/iv/v)	111(2)°	106 (2)°	118(2)°
O3-i(ii)—Ga^I— O3-iv(v)	107(3)°	99(3)°	114(3)°
$Ga^{II}O_4$ tetrahedra			
Ga^{II}-O1	1.79(5)	1.72(4)	1.87(4)
Ga^{II}-O2	1.93(6)	1.76(6)	2.10(7)
Ga^{II}-O3	1.84(5)	1.70(5)	1.98(5)
O1-i—Ga^{II}— O2-i	120(2)°	117.5(19)°	124(2)°
O1-i—Ga^{II}— O3-iv/viii	121(2)°	115(2)°	130(2)°
O2-i—Ga^{II}— O3-i	95(3)°	81(4)°	110(3)°
O2-i—Ga^{II}— O3-viii	94(3)°	81(4)°	110(3)°
O3-iv—Ga^{II}— O3-viii	99(3)°	96(3)°	103(2)°

Symmetry codes : (i) *x*, *y*, *z*; (ii) *y*, -*x*, 1-*z* ; (iii) *x*, *y*, -1+*z* ; (iv)-*x*, -*y*, -1+*z* ; (v) –*y*, *x*, 1-*z* ; (vi) *x*, *y*, 1+*z* ; (vii) ½+*x*, ½-*y*, 1-*z* ; (viii) ½-*y*, ½-*x*, *z* ; *x*, *y*, *z* are the average atomic coordinates in space group $P\bar{4}2_1m$.

A-O bond variation. The *A*-O polyhedra are strongly influenced by the displacive modulation, and as bond lengths vary as a function of *t* and *u*, the oxygen coordination of the *A* cations changes: AO_6, AO_7 and AO_8 polyhedra are found in different parts of the structure, assuming *A*–O distances > 2.9Å are disregarded (See Figure 3). The change of *A* coordination is clearly reflected by deformation of the pentagonal rings (Figure 4). The largest variation is observed for the *A*-O2 (Δ~0.532Å at *u*=0) and *A*-O3 (Δ~0.339Å at *u*=0) bonds, while the shortest bonds are least perturbed (Figure 5). All the atom pairs exceeding 2.9Å are of the *A*-O3 type, and most of the *A*-O2 bonds are shorter than the presumptive La^{3+}-O^{2+} bond length of 2.56 Å (according to the ionic radii of Shannon).[29]
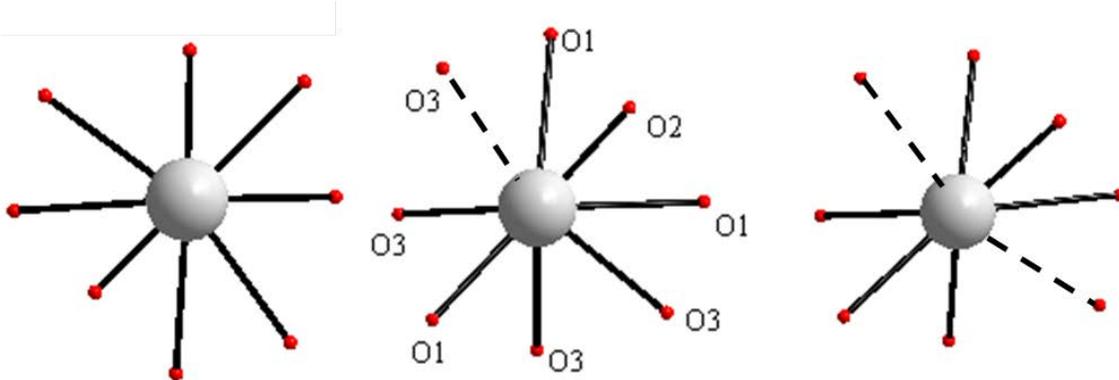
Figure 3. Examples of 8-, 7-, and 6-coordinated AO polyhedra where dashed lines represent atom pairs exceeding 2.9Å and excluded from the coordination sphere.
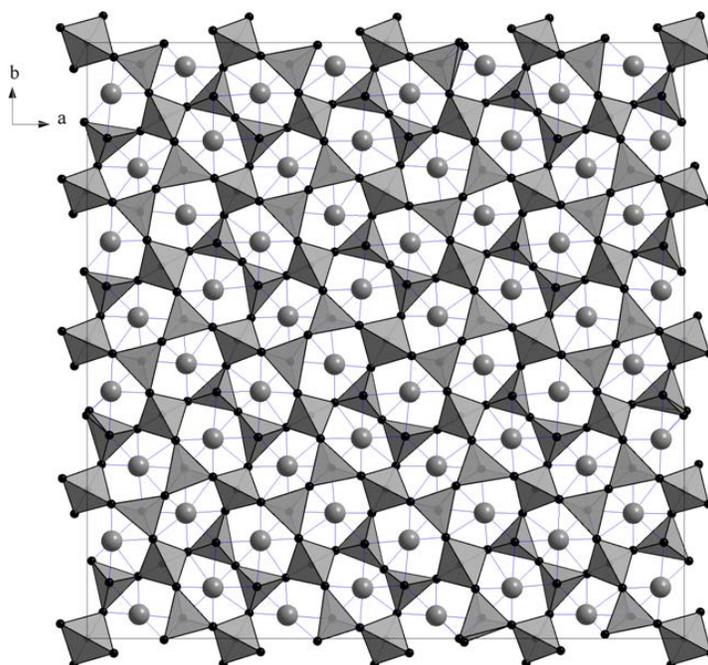

Figure 4. A portion of modulated structure projected along the c axis; 6-, 7- and 8-fold coordination gives rise to obvious deformation of the pentagonal rings. Bonds < 2.9Å are represented by solid lines.
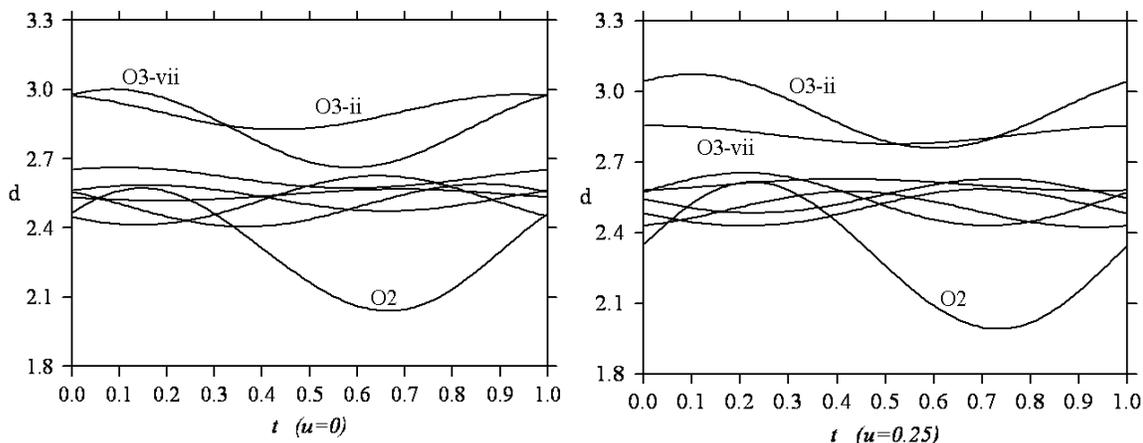
Figure 5. *A*-O bond variation (Å) as a function of *t* and *u*. Some of the *A*-O3 bonds exceed 2.9Å. Symmetry code is as given in Table 3.

Tetrahedral distortion. Bending and distortion of the $Ga^{II}_2O_7$ tetrahedral dimer is accommodated by the distortion of Ga^IO_4 (Figure 6). In the average structure, the Ga^I-O3 bond is a fixed length of 1.8325(10) Å, however, modulation permits variation from 1.63(5) Å to 2.04(5) Å (Figure 7). The O3-Ga^I-O3 bond angles show the largest deviation (11.91(2) °) from the average tetrahedral angle of 110.922(10)°, but this is much smaller than found in the comparable $[CaNd]_2[Ga]_2[Ga_2O_7]_2$ analogue (21.50(11)°), indicating less angular distortion of Ga^IO_4 tetrahedra. By comparison, the $Ga^{II}O_4$ tetrahedra are more regular with the largest departure from ideal shown for the O2-i—Ga^{II}—O3-i angle and the Ga^{II}-O2 bonds, with variation of ~15.33(5)° from 94.665° and up to 0.19(11)Å from the bond length observed in the average 3D structure (Figure 8). The smaller distortion of tetrahedra in $[CaLa]_2[Ga]_2[Ga_2O_7]_2$ is also consistent with the amplitude modulation vector being less than in $[CaNd]_2[Ga]_2[Ga_2O_7]_2$ (α~0.2319).[22]

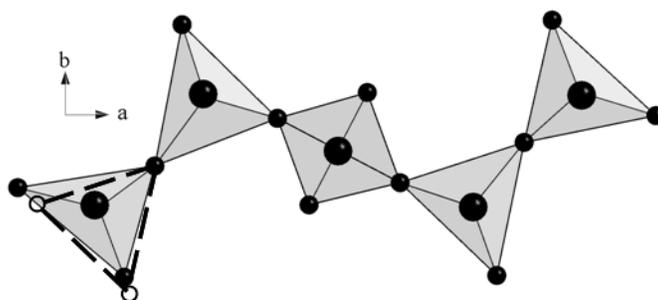Figure 6. GaO$_4$ tetrahedral distortion viewed along c direction. The dashed lines represent the ideal position of the tetrahedron. Bending of Ga$^{II}_2$O$_7$ tetrahedral dimers and distortion of GaO$_4$ tetrahedra can be observed.

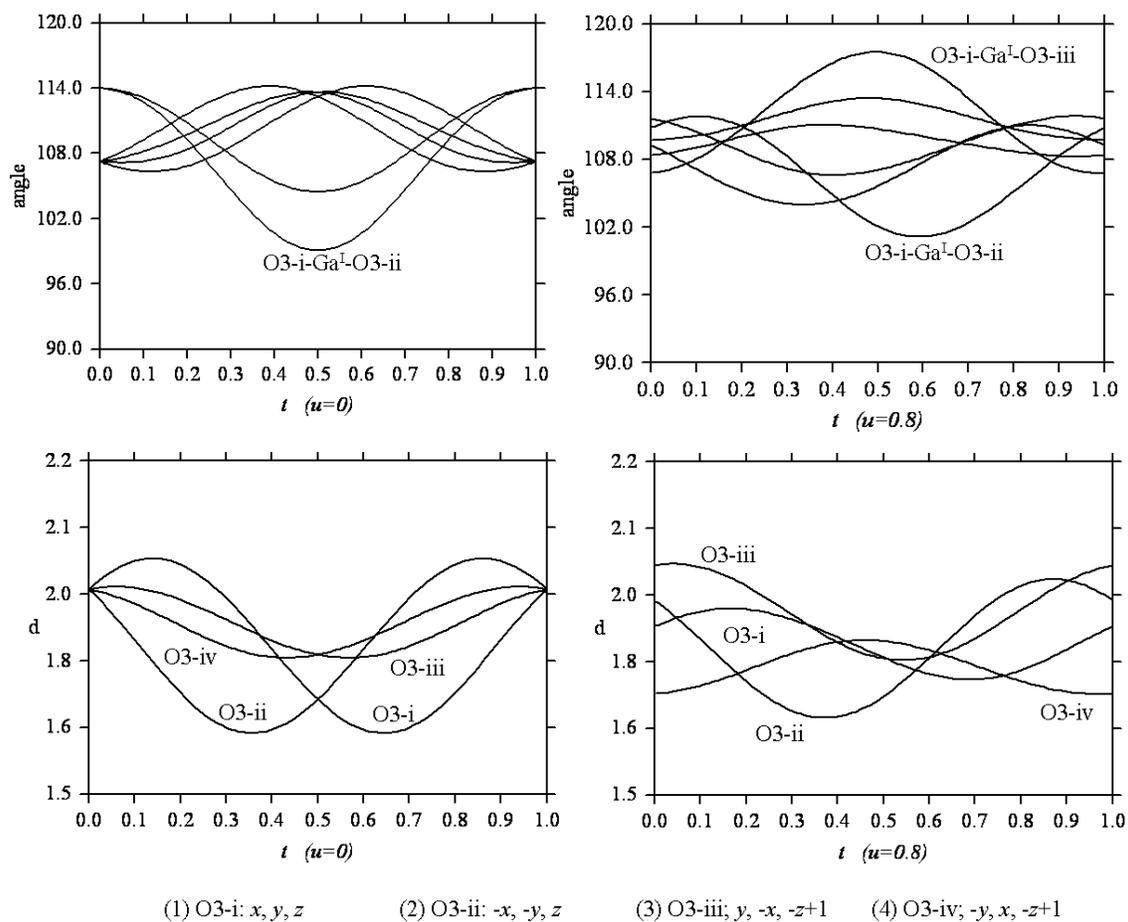(1) O3-i: x, y, z (2) O3-ii: $-x, -y, z$ (3) O3-iii; $y, -x, -z+1$ (4) O3-iv; $-y, x, -z+1$

Figure 7. Ga^I-O3 bond length (Å) and angle variation as a function of t at u=0 and u=0.8.
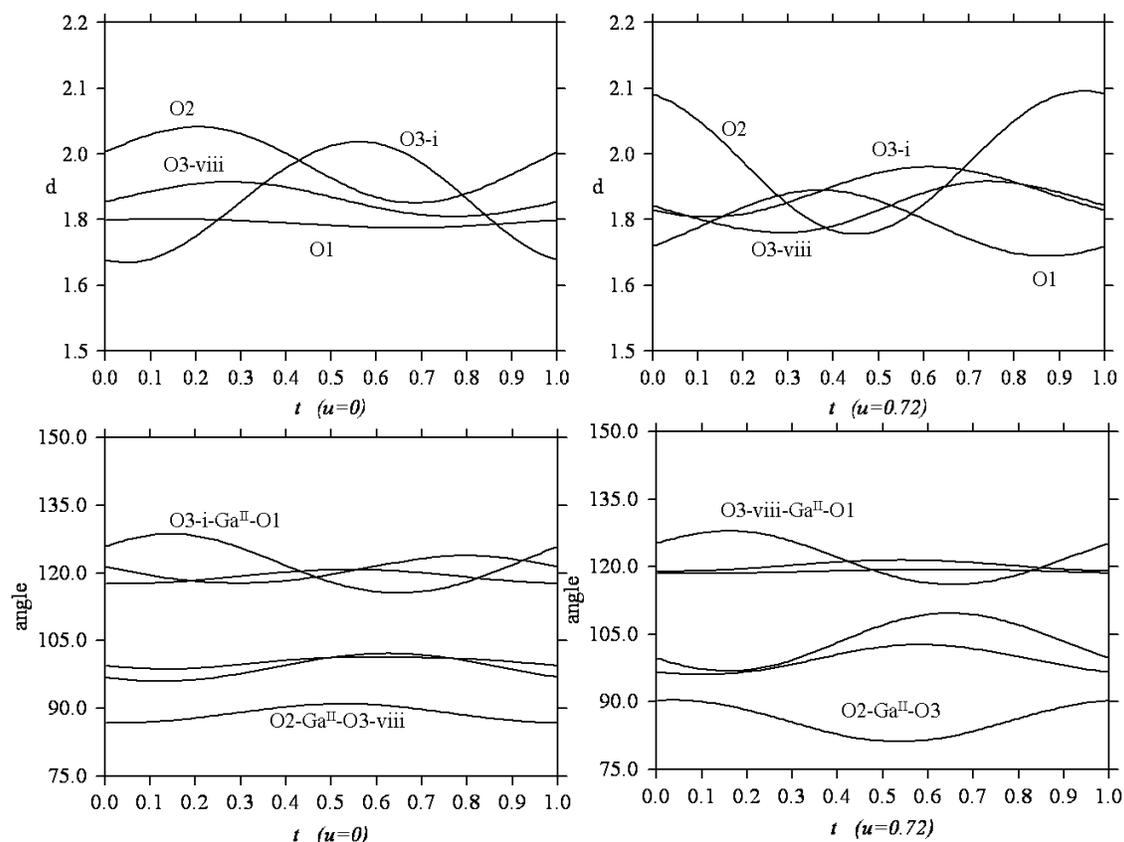
Figure 8. Ga^{II}-O bond length (Å) and angle variation as a function of t at u=0 and u=0.72. At u=0, the most remarkable variation occurs of the Ga^{II}-O3-i bond, and at u=0.72, on Ga^{II}-O2.

Occupancy modulation. Modulation causes the occupancy of La to extend from 0.464(2) to 0.503(3), and conversely Ca from 0.497(3) to 0.536(2) to yield a structural composition of [Ca$_{1.033}$La$_{0.967}$]$_2$[Ga]$_2$[Ga$_2$O$_7$]$_2$. Compositional variation is less significant than reported in [CaNd]$_2$[Ga]$_2$[Ga$_2$O$_7$]$_2$, where Nd content changes by more than 10% across the structure.[22] As expected, Ca-rich areas are dominant (Figure 9). Due to the minor compositional change, structural models with/without occupancy modulation do not strongly influence the atomic displacement and bond valence summations.
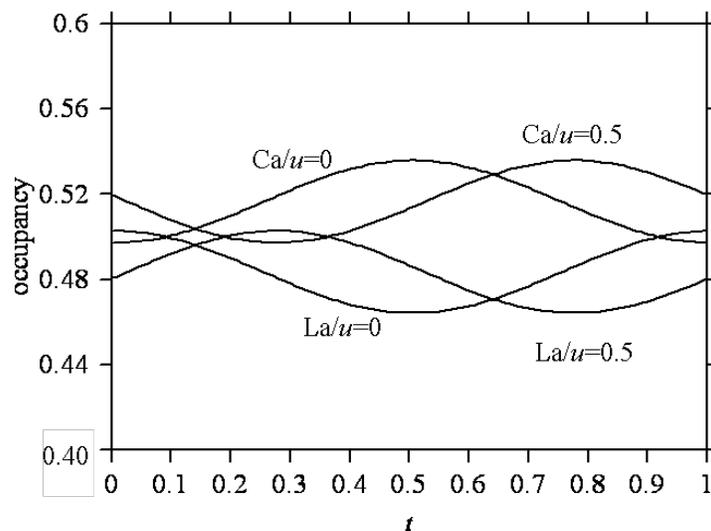
16

Figure 9. Ca/La occupancy modulation as a function of *t* at *u*=0 and *u*=0.5.

Bond valence summations (BVS). Using the parameters of Altermatt & Brown,[30] the BVS of Ca/La were obtained by summing the partial bond valence of Ca and La through the occupancy ratios along *t* and *u*. Table 4 lists the BVS for all cations for the average and modulated structures. Similar to the incommensurate structure of $[CaNd]_2[Ga]_2[Ga_2O_7]_2$ the values for Ca/La are significantly lower than the formal average charge, consistent with the interstices being too large for the AO_8 site cations, and for this reason 6- and 7-fold coordination is evident. However, $[CaLa]_2[Ga]_2[Ga_2O_7]_2$ gives better *A* site BVS (mean value 2.30) than $[CaNd]_2[Ga]_2[Ga_2O_7]_2$ (mean value 2.09),[22] as the larger ionic radius of La narrows bond length variation. Both the occupational modulation and the *A*-O bond length variation contribute to the large *A* site BVS variation; with the latter gives larger influences, since the occupational modulation between Ca/La is small. The BVS values show large variations, but their mean values are tolerable (Figure 10), and in fact, the mean values for all cations in the modulated structure are closer to the formal values than those derived from the average structure.

Table 4. Bond Valence Sums

	Formal value	Average structure	Modulated structure		
			Mean value	Minimum	Maximum
Ca/La	2.47	2.08(10)	2.30(3)	1.88(10)	3.02(2)
Ga^I	3	3.15(3)	3.10(20)	2.17(2)	3.71(3)
Ga^{II}	3	3.17(2)	3.02(10)	2.70(2)	3.22(3)
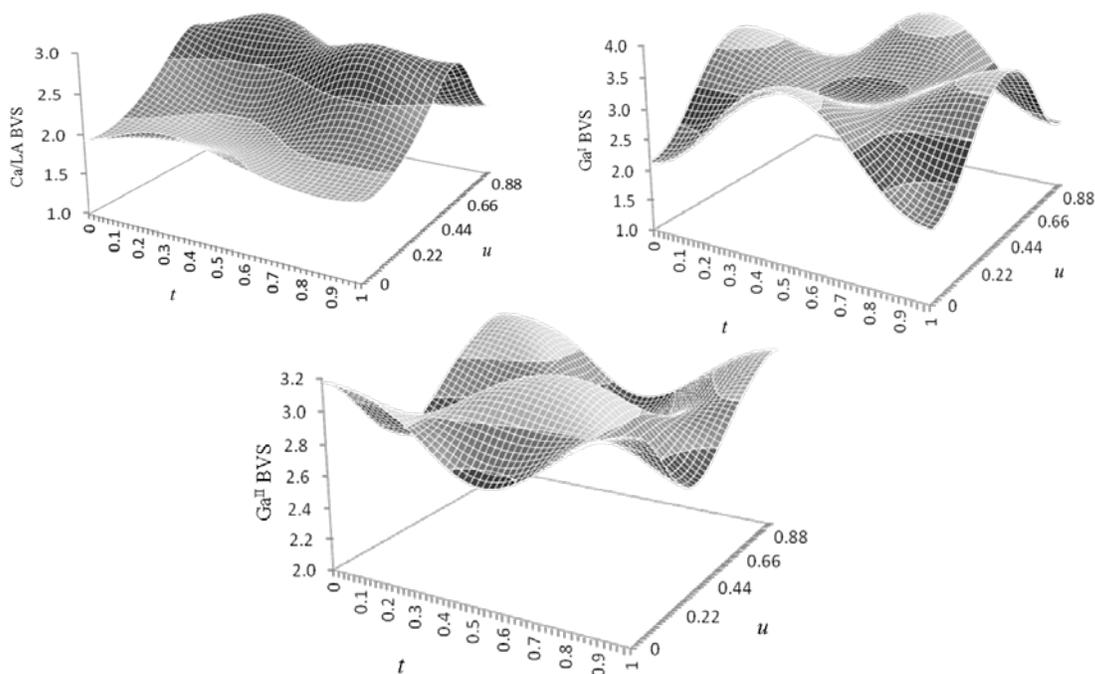
Figure 10. BVS for all cations in the modulated $[CaLa]_2[Ga]_2[Ga_2O_7]_2$.

Temperature dependence. Variable temperature single crystal X-ray diffraction showed the magnitude of the modulation vectors α decreases from 0.2247(6) to 0.2160(4) by warming from 100K to 293K (Figure 11), which is much less than recorded for the melilite analogue $[Ca]_2[Co_{0.9}Zn_{0.1}]_2[Si_2O_7]_2$ (0.33≤α≤0.29).[31] At elevated temperature, modulation becomes weaker, possibly as the larger ADPs of Ca/La, more effectively fill the interstices and reduce the stress of interlayer misfit. A

commensurate-incommensurate phase transition was not observed across this temperature range as reported earlier for natural $[Ca_{1.89}Sr_{0.01}Na_{0.08}K_{0.02}]_2[Mg_{0.92}Al_{0.08}]_2[Si_{1.97}Al_{0.03}O_7]_2$ and synthetic $[(Sr/Ca)]_2[(Co/Mg/Zn/Fe/Cu)]_2[(Si/Ge)_2O_7]_2$ compositions.[14, 32] It is of interest that the strontium analogue $[SrLa]_2[Ga]_2[Ga_2O_7]_2$ does not have satellite reflections even when the temperature drops to 100K, and the reasons for this will be examined in a forthcoming publication.
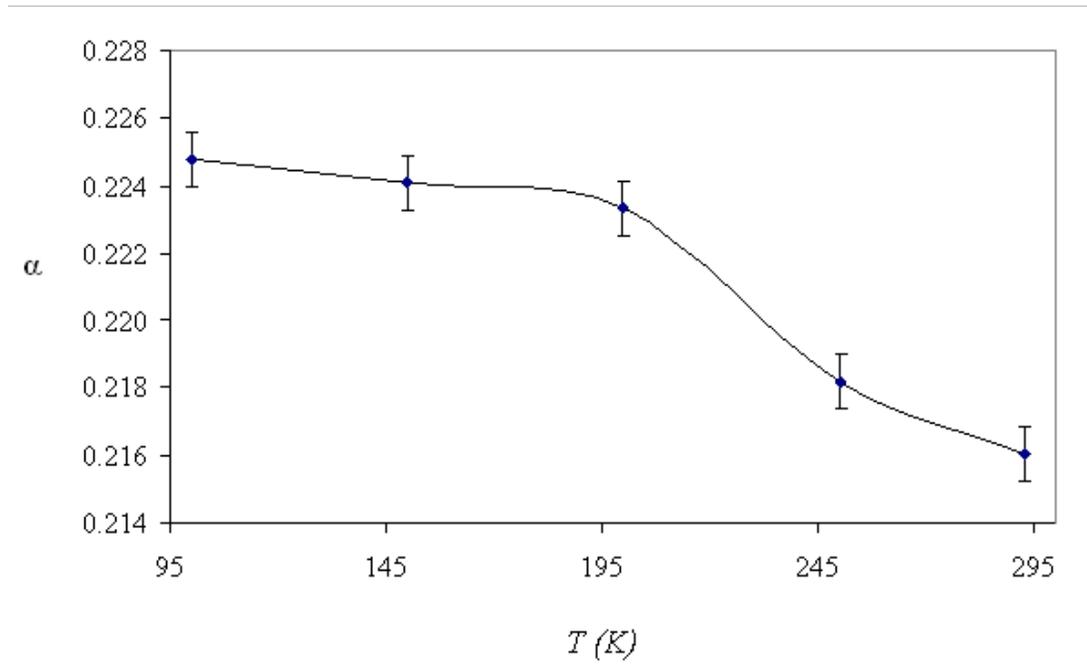

Figure 11. Temperature effect on modulation vectors, the magnitude α decreases with the increase of temperature (from 100K to room temperature).

Compositional effect on modulation. The modulation vectors q_1/q_2 are most obviously affected by the size of the A and B^I/B^{II} cations. SAED shows that increasing the La/Ca atomic ratio, leads to an abrupt decrease of satellite intensity for La/Ca = 1.1/0.9 (Figure 2), and these reflections become undetectable when La/Ca > 1.3/0.7; nevertheless, more sensitive detection methods such as electron imaging plates may reveal their presence.

This reduction in intensity is attributable to the increase of $A\!:\!B^I/B^{II}$ ionic radius ratio as La content increases, which better fits the interlayer interstice and reduces the structural distortion. Consistent with this, the interstice volume decreases for La/Ca=1.5/0.5 (volume ~29.87Å^3) while the average A cation size increases. In order to systematize the influence of interlayer cations, the modulation vectors and the A/B^I radius ratios for a variety of B^{II} are summarized in Figure 12. Selected melilite compositions are listed in Table 5. For different $B^{II}_2O_7$, changing the combination of A and B^I regulates the adoption of modulated or non-modulated structures (near room temperature), such that the A/B^I ratio is normally smaller for incommensurate melilite. For example, in $[A_2]_2[B^I]_2[Si_2O_7]_2$ silicates, the modulated A/B^I is below ~2.1, while for the $[A_2]_2[B^I]_2[Ga_2O_7]_2$ gallates, this value is around 2.4. The open circle represents $[Sr_2]_2[Mn]_2[Ge_2O_7]_2$, whose crystallographic dimensions are not yet established, but on the basis of our analysis, it is expected to be incommensurate.

Table 5. Selected melilite compositions.

|	Melilite	A/B^I	B^{II} radii	reference
Modulated structure (at room temperature)	$[CaLa]_2[Ga]_2[Ga_2O_7]_2$	2.426	0.47	this study
	$[CaNd]_2[Ga]_2[Ga_2O_7]_2$	2.383	0.47	[22]
	$[Ca_2]_2[Ga]_2[GaGeO7]_2$	2.383	0.43	[22]
	$[Ca_2]_2[Mg]_2[Si_2O_7]_2$	1.965	0.26	[18]
	$[Ca_2]_2[Co]_2[Si_2O_7]_2$	2.000	0.26	[17, 19]
	$[Ca_2]_2[Zn]_2[Si_2O_7]_2$	1.867	0.26	[18]
	$[Ca_2]_2[Mg_{0.4}Fe_{0.6}]_2[Si_2O_7]_2$	1.848	0.26	[14]
	$[Ca_2]_2[Zn]_2[Ge_2O_7]_2$	1.867	0.39	[14]
	$[Ca_{1.74}Sr_{0.26}]_2[Co]_2[Si_2O_7]_2$	2.033	0.26	[20, 21]
unknown	$[Sr_2]_2[Mn]_2[Ge_2O_7]_2$	1.909	0.39	
Non-modulated (at room temperature)	$[Sr_2]_2[Mg]_2[Si_2O_7]_2$	2.211	0.26	[14]
	$[Sr_2]_2[Zn]_2[Si_2O_7]_2$	2.100	0.26	[14]
	$[Ca_2]_2[Al]_2[Si_2O_7]_2$	2.872	0.26	this study
	$[CaLa]_2[Al]_2[Al_2O_7]_2$	2.923	0.39	this study
	$[CaNd]_2[Al]_2[Al_2O_7]_2$	2.872	0.39	this study
	$[SrNd]_2[Ga]_2[Ga_2O_7]_2$	2.532	0.47	this study
	$[SrLa]_2[Ga]_2[Ga_2O_7]_2$	2.574	0.47	this study
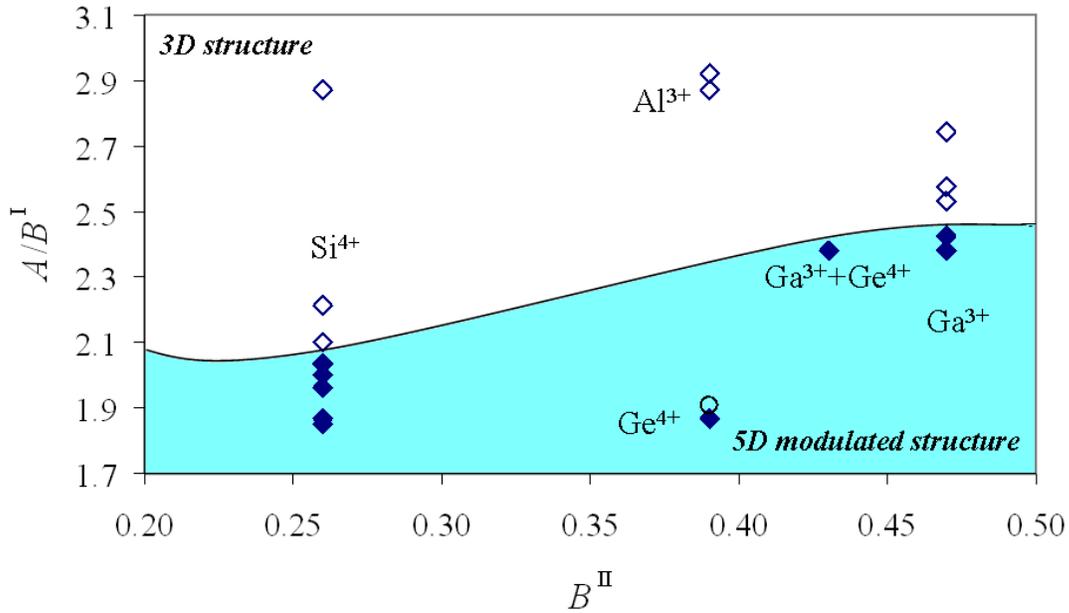
Figure 12. Correlation of composition with modulation for melilites.[14, 17-21, 33] Analysis is conducted by considering the radius ratio A/B^I with respect to the B^{II} size. The solid spots represent incommensurate structures. The ionic radii are from Shannon.[34]

5. Conclusion

In melilites, the fundamental driver towards modulation is size misfit between the interlayer space and occupying cations. Specifically, incommensurate modulation is expected when La/Ca is replaced by smaller lanthanides (Gd, Sm), or a larger cation fills the tetrahedral site (such as Fe, Zn). Even without modulation, the two-dimensional tetrahedral network of the type $[(3.5.4.5)^2, 3.5.3.5]^{35}$ contains pentagons that geometrically predicate distortion to allow space filling. For example, [SrLa]$_2$[Ga]$_2$[Ga$_2$O$_7$]$_2$ and [SrNd]$_2$[Ga]$_2$[Ga$_2$O$_7$]$_2$ are not modulated at room temperature, but the anion-net is significantly different to the underlying semi-regular network. The deformations are most evident in the incommensurate forms (e.g.

21

$[CaLa]_2[Ga]_2[Ga_2O_7]_2$, $[CaNd]_2[Ga]_2[Ga_2O_7]_2$[22]). Such long range distortion is enabled by twisting of the 2D anion array, that is a prerequisite for high interstitial oxygen mobility, and results in very low oxygen migration excitation energies. A key advantage of ionic conductors where mobility is mediated by excess oxygen is the ease of migration. By way of comparison, the activation energy of $[Sr_{0.46}La_{1.54}]_2[Ga]_2[Ga_2O_{7.27}]_2$ is 0.42eV at 600-900°C, and for $[Ca_{0.36}La_{1.64}]_2[Ga]_2[Ga_2O_{7.32}]_2$ 0.45eV above 650°C.[12, 13] On the other hand, most other ionic conductors that rely on an interstitial diffusion mechanism show higher activation barriers (e.g. 0.56eV for lanthanum silicate apatite)[2, 36-38] Modulation is favored by increasing the $A:B^I/B^{II}$ ionic radius ratio, that in turn delivers lower activation energies and enhances the oxygen migration. Quantitative crystallographic analyses, including higher dimensional features, are crucial to describing oxygen diffusion in melilite. Furthermore, mapping the large anisotropic displacements of oxygen provides guidance for predicting the possible diffusion pathway for oxide ion conduction, which can be subsequently verified through molecular dynamic simulations.[39]

Supporting information available: The CIF for average and modulated structure [CaLa]$_2$[Ga]$_2$[Ga$_2$O$_7$]$_2$. This material is available free of charge at http://pubs.acs.org.

Corresponding Author:

*Division of Materials Science & Engineering, Nanyang Technological University, Singapore.

 Email: weif0002@ntu.edu.sg;

tjwhite@ntu.edu.sg

1.   Minh, N. Q., Ceramic fuel-cells. *J. Am. Ceram. Soc* **1993,** 76, (3), 563-588.
2.   Goodenough, J. B., Oxide-ion conductors by design. *Nature* **1999,** 404, 821-822.
3.   Lacorre, P.; Goutenoire, F.; Bohnke, O.; Retoux, R.; Laligant, Y., Designing fast oxide-ion conductors based on La$_2$Mo$_2$O$_9$. *Nature* **2000,** 404, 856-858.
4.   Boivin, J. C., Structural and electrochemical features of fast oxide ion conductors. *Int. J. Inorganic Materials* **2001,** 3, 1261-1266.
5.   Jacobson, A., Materials for Solid Oxide Fuel Cells. *Chem. Mater* **2010,** 22, 660-674.
6.   Kendrick, E.; Islam, M. S.; Slater, P. R., Developing apatites for solid oxide fuel cells: insight into structural transport and doping properties. *J. Mater. Chem.* **2007,** 17, 3104-3111.
7.   Pramana, S. S.; Baikie, T.; Kendrick, E.; Schreyer, M. K.; Slater, P. R.; White, T. J., Crystal chemistry and optimization of conductivity in 2*A*, 2*M* and 2*H* alkaline earth lanthanum germanate oxyapatite electrolyte polymorphs. *Solid State Ionics* **2010,** 181, 1189-1196.
8.   Packer, R. J.; Tsipis, E. V.; Munnings, C. N.; Kharton, V. V.; Skinner, S. J.; Frade, J. R., Diffusion and conductivity properties of cerium niobate. *Solid State Ionics* **2006,** 177, 2059-2064.
9.   Pramana, S. S.; Klooster, W. T.; White, T. J., Framework 'interstitial' oxygen in La$_{10}$(GeO$_4$)$_5$(GeO$_5$)O$_2$ apatite electrolyte. *Acta Crystallogr. B* **2007,** 63, 597-602.
10.   Hamdi, B.; El Feki, H.; Salah, A. B.; Salles, P.; Baules, P.; Savariault, J.-M., Ionic conductivity and phase transition in Pb$_{4.8}$Bi$_{1.6}$Na$_{3.6}$(PO$_4$)$_6$, an apatite-type compound. *Solid State Ionics* **2006,** 177, 1413-1420.
11.   Orera, A.; Baikie, T.; Kendrick, E.; Shin, J. F.; Pramana, S.; Smith, R.; White, T. J.; Sanjuan, M. L.; Slater, P. R., Apatite genmanates doped with tungsten: synthesis, structure and conductivity. *Dalton Trans* **2011,** 40, 3903-3908.

12.   Kuang, X. J.; Green, M. A.; Niu, H. H.; Zajdel, P.; Dickinson, C.; Claridge, J. B.; Jantsky, L.; Rosseinsky, M. J., Interstitial oxide ion conductivity in the layered tetrahedral network melilite structure. *Nature Mater.* **2008,** 7, 498-504.

13.   Li, M. R.; Kuang, X. J.; Chong, S. Y.; Xu, Z. L.; Thomas, C. I.; Niu, H. J.; Claridge, J. B.; M.J., R., Interstitial oxide ion order and conductivity in $La_{1.64}Ca_{0.36}Ga_3O_{7.32}$ melilite. *Angew. Chem. Int. Ed.* **2010,** 49, 2362 -2366.

14.   Rothlisberger, F.; Seifert, F.; Czank, M., Chemical control of the commensurate-incommensurate phase transition in synthetic melilites. *Eur. J. Mineral.* **1990,** 2, 585-594.

15.   Bindi, L.; Bonazzi, P.; Dusek, M.; Petricek, V.; Chapuis, G., Five-dimensional structure refinement of natural melilite, $(Ca_{1.89}Sr_{0.01}Na_{0.08}K_{0.02})(Mg_{0.92}Al_{0.08})(Si_{1.98}Al_{0.02})O_7$. *Acta Crystallogr. B* **2001,** 57, 739-746.

16.   Merwin, L. H.; Sebald, A.; Seifert, F., The incommensurate-comensurate phase transition in akermanite $Ca_2MgSi_2O_7$, . *Phys. Chem. Miner.* **1989,** 16, 752-756.

17.   Hagiya, K.; Ohmasa, M., The modulated structure of synthetic Co-Akermanite, $Ca_2CoSi_2O_7$. *Acta Crystallogr. B* **1993,** 49, 172-179.

18.   Tamura, T.; Yoshiasa, A.; Iishi, K.; Takeno, S.; Maeda, H.; Emura, S.; Koto, K., Local structure of $(Ca, Sr)_2 (Mg, Co, Zn)Si_2O_7$ melilite solid-solution with modulated structure. *Phys. Chem. Miner.* **1996,** 23, 81-88.

19.   Yang, H.; Hazen, R. M.; Downs, R. T.; Finger, L. W., Structural change associated with the incommensurate-normal phase transition in akermanite, $Ca_2MgSi_2O_7$, at high pressure. *Phys. Chem. Miner.* **1997,** 24, (Springer-Verlag), 510-519.

20.   Jiang, J. C.; Schosnig, M.; Schaper, A. K.; Ganster, K., Modulations in incommensurate $(Ca_{1-x}Sr_x)_2MgSi_2O_7$ single crystals. *Phys. Chem. Miner.* **1998,** 26, (Springer-Verlag), 128-134.

21.   Bagautdinov, B.; Hagiya, K.; Kusaka, K.; Ohmasa, M.; Iishi, K., Two dimensional incommensurately modulated structure of $(Sr_{0.13}Ca_{0.87})_2CoSi_2O_7$ crystals. *Acta Crystallogr. B* **2000,** 56, 811-821.

22.   Wei, F. X.; Baikie, T.; An, T.; Shreyer, M.; Kloc, C.; White, T., Five-Dimensional Incommensurate Structure of the Melilite Electrolyte $[CaNd]_2[Ga]_2[Ga_2O_7]_2$. *J. Am. Chem. Soc.* **2011,** 133, (38), 15200-15211.

23.   Stokes, H. T.; Campbell, B. J.; van Smaalen, S., Generation of (3 + d)-dimensional superspace groups for describing the symmetry of modulated crystalline structures. *Acta Crystallogr. A* **2011,** 67, 45-55.

24.   Petricek, V.; Dusek, M.; Palatinus, L. *Jana2006. The crystallographic computing system.*, Institute of Physics, Praha, Czech Republic, 2006.

25.   Sears, V. F., *International Tables for Crystallography*. Academic Publishers: Dordrecht, Kluwer, 1993.

26.   Li, L.; Wolfel, A.; Schonleber, A.; Mondal, S.; Schreurs, A.; Kroon-Batenburg, L.; van Smaalen, S., Modulated anharmonic ADPs are instrinsic to aperiodic crystals: a case study on incommensurate Rb_2ZnCl_4. *Acta Cryst. B* **2010,** 67, 205-217.

27.   Pramana, S. S.; White, T. J.; Schreyer, M. K.; Ferraris, C.; Slater, P. R.; Orera, A.; Bastow, T. J.; Mangold, S.; Doyle, S.; Liu, T.; Fajar, A.; Srinivasan, M.; Baikie, T., Pseudomorphic 2A --> 2M --> 2H Phase Transitions in Lanthanum Strontium Germanate Electrolyte Apatites. *Dalton Trans.* **2009**, 8280-8291.

28.   Tsipis, E. V.; Munnings, C. N.; Kharton, V. V.; Skinner, S. J.; Frade, J. R., Transport properties and structural stability of tetragonal $CeNbO_{4+\delta}$. *Solid State Ionics* **2006,** 177, 1015-1020.

29.   Shannon, R. D., *Acta Crystallogr. A* **1976,** 32.

30.   Altermatt , D.; Brown, I. D., *Acta Crystallogr. B* **1985,** 41, 244-247.

31.   Jia, Z. H.; Schaper, A. K.; Massa, W.; Treutmann, W.; Rager, H., Structure and phase transition in $Ca_2CoSi_2O_7$-$Ca_2ZnSi_2O_7$ solid solution crystals. *Acta Crystallogr. B* **2006,** 62, 547-555.

32.   Bindi, L.; Bonazzi, P., Incommensurate-normal phase transition in natural melilite: an in situ high temperature X-Ray single crystal study. *Phys. Chem. Miner.* **2005,** 32, 89-96.

33.   Skakle, J. M. S.; Herd, R., Crystal chemistry of (RE, A)$_2$ M$_3$ O$_7$ compounds (RE= Y, lanthanide; A= Ba, Sr, Ca; M= Al, Ga). *Powder Diffraction* **1999,** 14, 195-202.

34.   Shannon, J.; Katz, L., The structures of the reduced and oxidized forms of barium silicon tantalum oxide, $Ba_3Si_4Ta_6O_{23}$ and $Ba_3Si_4Ta_6O_{26}$. *J. Solid State Chem.* **1970,** 1, 399-408.

35.   O'Keeffe, M.; Hyde, B. G., Plane nets in crystal chemistry. *A mathematical and physical science* **1980,** 295, 553-623.

36.   Tsai, D.; Hsieh, M.; Tseng, J.; Lee, H., Ionic conductivities and phase transitions of Lanthanide rare-earth substituted $La_2Mo_2O_9$. *J. Eur. Ceramic Society* **2005,** 25, 481-487.

37.   Yoshioka, H., Oxide ionic conductivity of apatite-type lanthanum silicates. *J. all. com* **2006,** 408-412, 649-652.

38.   Tolchard, J. R.; Islam, M. S.; Slater, P. R., Defect chemistry and oxygen ion migration in the apatite-type materials $La_{9.33}Si_6O_{26}$ and $La_8Sr_2Si_6O_{26}$. *J. Mater. Chem.* **2003,** 13, 1956-1961.

39.   Tealdi , C.; Mustarelli , P.; Islam, M. S., Layered $LaSrGa_3O_7$ -based oxide-ion conductors: cooperative transport mechanisms and flexible structures. *Adv. Funct. Mater.* **2010,** 20, (22), 3874-3880.

Table of Content Graphic
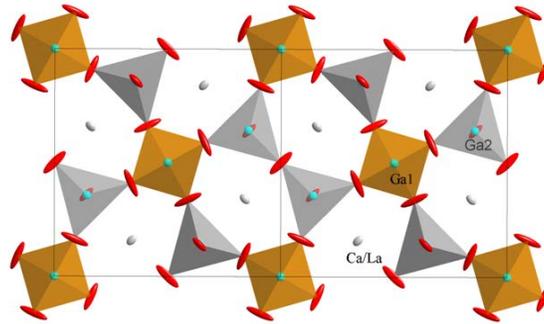
The average structure of $[CaLa]_2[Ga]_2[Ga_2O_7]_2$ viewed along c axis. This gallate melilite-type solid electrolyte is incommensurate. The large anisotropic displacements reflect the high oxygen mobility in these materials and crystal chemistry can be adjusted to optimize performance